Journal of Biomechanics 61 (2017) 1–10

Contents lists available at ScienceDirect

Journal of Biomechanics

journal homepage: www.elsevier.com/locate/jbiomech
www.JBiomech.com

Consistent trilayer biomechanical modeling of aortic valve leaflet tissue

Ahmed A. Bakhaty [a,c], Sanjay Govindjee [b], Mohammad R.K. Mofrad [c,*]

[a] Departments of Civil & Environmental Engineering and Electrical Engineering & Computer Science, University of California, Berkeley, United States
[b] Department of Civil & Environmental Engineering, University of California, Berkeley, United States
[c] Molecular Cell Biomechanics Laboratory, Departments of Bioengineering and Mechanical Engineering, University of California, Berkeley, United States

ARTICLE INFO

Article history:
Accepted 5 June 2017

Keywords:
Aortic valve
Fiber micromechanics
Anisotropy
Multiscale
Multiphysics

ABSTRACT

Aortic valve tissue exhibits highly nonlinear, anisotropic, and heterogeneous material behavior due to its complex microstructure. A thorough understanding of these characteristics permits us to develop numerical models that can shed insight on the function of the aortic valve in health and disease. Herein, we take a closer look at consistently capturing the observed physical response of aortic valve tissue in a continuum mechanics framework. Such a treatment is the first step in developing comprehensive multiscale and multiphysics models.

We highlight two important aspects of aortic valve tissue behavior: the role of the collagen fiber microstructure and the native prestressing. We propose a model that captures these two features as well as the heterogeneous layer-scale topology of the tissue. We find the model can reproduce the experimentally observed multiscale mechanical behavior in a manner that provides intuition on the underlying mechanics.

1. Introduction

Aortic valve (AV) disease is a public health concern with no effective treatment options available, due in part to our incomplete understanding of the complex biological system. Computational modeling is a promising approach for us to gain insight on AVs and to develop viable prevention and treatment modalities. However, such modeling must first accurately reproduce the known before we can use it to probe the unknown. Our focus here is to discuss critical aspects of developing a continuum biomechanical model of AV tissue that is consistent with available experimental data. This basic material specification is a fundamental building block for more complex and comprehensive AV studies, such as multiscale and multiphysics simulations.

1.1. Background

AV tissue is comprised of three layers: the fibrosa, the ventricularis, and the spongiosa. The fibrosa and the ventricularis are the main load-bearing layers and they consist of organized networks of collagen and elastin fibers. The crimped collagen fibers align, uncrimp and quickly stiffen in response to loading, resulting in the observed anisotropic, exponential stress-strain behavior. The highly compliant spongiosa serves as a buffer between the other two layers and is composed of proteoglycans. Little data is available on the mechanical behavior of the spongiosa, but the three layers act together as a single unit (Sacks and Yoganathan, 2007).

Typical continuum models of AV tissue assume homogeneous materials that aim to capture the gross mechanical response; see e.g. Katayama et al. (2013), Labrosse et al. (2011), Weinberg et al. (2009), Weinberg and Kaazempur Mofrad (2008) and Weinberg and Mofrad (2007), as well as Bakhaty and Mofrad (2015) and Weinberg et al. (2010) for reviews. Fewer studies look at the heterogeneous nature of the trilayer AV structure; see for instance Weinberg and Mofrad (2007), and Buchanan and Sacks (2014). This heterogeneity is essential for correct multiscale modeling efforts (Vesely, 1997; Sacks et al., 1998; Huang et al., 2007). Such models rely upon layer-scale (and possibly finer scale) measurements that can be incorporated into detailed composite models that predict the behavior of intact AV tissue. The consistency of the layer level response model and the composite tissue model is essential for the validity of the entire exercise and a major goal of this paper.

1.2. Aortic valve tissue biomechanics

To understand the heterogeneous layer-scale and composite AV tissue behavior, Stella and Sacks (2007) subjected excised AV tissue samples to equibiaxial tractions along the "circumferential" and

* Corresponding author.
E-mail addresses: abakhaty@berkeley.edu (A.A. Bakhaty), s_g@berkeley.edu (S. Govindjee), mofrad@berkeley.edu (M.R.K. Mofrad).

http://dx.doi.org/10.1016/j.jbiomech.2017.06.014
0021-9290/

"radial" axes.[1] The layers (fibrosa and ventricularis) were then separated and tested individually. The average load-response curve for each layer and the AV composite tissue is reproduced in Fig. 1. We highlight the following from the experiments:

1. The tissue is highly anisotropic: the circumferential response being significantly stiffer than the radial (due to the gross alignment of the collagen fibers in the circumferential direction (Balguid et al., 2008). Additionally, the fibrosa is significantly stiffer than the ventricularis.
2. At the layer-scale, we observe a "kickback" behavior in the circumferential direction, characterized by a *decrease* in stretch with increasing load.
3. After separation, the fibrosa expands, while the ventricularis contracts, indicating the existence of a prestress in the native AV tissue.
4. Interconnecting fibers that run transmurally (longitudinally/axially) are believed to cause the AV tissue composite to act as a single unit (see also Buchanan and Sacks, 2014).
5. The composite AV response in the radial direction is *stiffer* than the individual layers in the same direction. Note the stiffness in Fig. 1 may be misleading due to the use of membrane stress, but when correcting for the relative size of the individual and composite samples, the conclusion remains.

Our aim is to develop a model that captures the observed mechanical response of the AV tissue composite within a continuum mechanics framework, based upon layer-scale models which are calibrated to layer-scale measurements.

We restrict our attention to the equibiaxial data presented in Stella and Sacks, as opposed to more general biaxial experiments[2] (Billiar and Sacks, 2000b). The latter study lacks data on the individual layers and it is our goal here to capture layer-scale consistency. We do, however, consider the bending experiment of Sacks (2001) to calibrate the small-strain response of the material.

1.3. Outline

The article is outlined as follows. In Section 2 we introduce the modeling framework which we calibrate to existing experimental data in Section 3. We conclude with a discussion, including limitations, in Section 4.

2. Methods

2.1. Continuum mechanics framework

We model the AV tissue within a classical continuum mechanics framework (see e.g., Holzapfel, 2000), wherein we seek to solve the governing equations of motion for a body (manifold with boundaries) subject to boundary conditions (tractions and displacements). We define a one parameter (time t) family of finite deformation maps $\boldsymbol{\varphi}_t : \mathbb{R}^3 \mapsto \mathbb{R}^3$ of a hyperelastic body (see Fung (1990) or Holzapfel (2000, Chap. 6)), as is typical in modeling biological tissue. The equilibrium deformation map at time t is the one that minimizes the potential energy (Π) of the elastic system subject to conservative traction loading $\bar{\boldsymbol{t}}_t$:

$$\boldsymbol{\varphi}_t^{eq} = \arg\inf_{\boldsymbol{\varphi}_t} \Pi(\boldsymbol{\varphi}_t, \bar{\boldsymbol{t}}_t). \tag{1}$$

Under the assumption of hyperelasticity, the 1st Piola-Kirchhoff stress of the system, $\boldsymbol{P}$, is obtained from the Helmholtz free energy, $\hat{\psi}$, of the material:

$$\boldsymbol{P} = \frac{\partial \hat{\psi}}{\partial \boldsymbol{F}}, \tag{2}$$

where $\boldsymbol{F} = \nabla\boldsymbol{\varphi}$ is the deformation gradient. Although the solution to (1) is in general not unique, polyconvexity (in the sense of Ball (1976)) of the energy function (along with appropriate growth conditions) guarantees the existence of a solution. We solve the problem with a standard Finite Element (FE) numerical procedure (Section 2.4). Our challenge is to specify $\hat{\psi}$ such that the FE model is consistent with the observed experimental response.

2.2. Material model

For each individual layer we choose a Helmholtz free energy $\psi(I_1, J_4, J) := \hat{\psi}(\boldsymbol{F})$ of the form

$$\psi = C_{1m}\{\exp[C_{2m}(I_1 - 3)] - 1\} + \sum_{i=1}^{n_f} \frac{C_{1f}}{2C_{2f}}\left\{\exp\left[C_{2f}(J_4^i - 1)_+^3\right] - 1\right\} + c_1(I_1 - 3) + c_2(J^2 - 1) + c_3 \ln(J). \tag{3}$$

The first term on the right hand side is a Fung-like (Fung, 1990) isotropic term, where $I_1 = \mathrm{tr}(\boldsymbol{F}^T\boldsymbol{F})$ is the first invariant, and C_{1m}, C_{2m} are material parameters. The second term is a directional term in the spirit of Holzapfel (Holzapfel et al., 2000; Holzapfel and Ogden, 2010) to account for the n_f collagen fiber directions, where $J_4^i = \mathrm{tr}(\boldsymbol{C}\boldsymbol{M}_i)$ is the first mixed invariant for the fiber direction indexed by i, with $\boldsymbol{M}_i = \boldsymbol{m}_i \otimes \boldsymbol{m}_i, ||\boldsymbol{m}_i||_2 = 1$, as the rank-1 structure tensor. C_{1f}, C_{2f} are material parameters and $(x)_+ := \max(x, 0)$ guarantees that the fibers do not take compressive load. The last three terms represent a Neo-hookean ground substance (see Gundiah et al., 2007) with parameters c_1, c_2, c_3. The following conditions must hold for the model to behave consistently as a linear elastic material at small deformations (see Appendix A):

$$c_1 = \mu/2 - C_{1m}C_{2m}, \quad c_2 = K/4 - \mu/6 - C_{1m}C_{2m}^2, \quad c_3 = 2C_{1m}C_{2m}^2 - K/2 - 2\mu/3, \tag{4}$$

where μ and K are the infinitesimal-strain shear and bulk moduli, respectively. Expressions for the Cauchy stress and material tangent are given in Appendix C. The parameter constraints,

$$C_{1m}, C_{2m}, C_{1f}, C_{2f}, c_1, c_2, -c_3 > 0, \tag{5}$$

ensure polyconvexity of (3); see Appendix B for details (Morrey, 1952; Dacorogna, 2007; Schröder and Neff, 2003).

In valve tissue, the collagen fibers are primarily aligned in the circumferential direction (Billiar and Sacks, 2000b). We define a locally *Cartesian* coordinate system (c, r, h) aligned with the circumferential, radial, and transmural directions, respectively (see Fig. 2 and/or Billiar and Sacks (2000b)). In the spirit of Billiar and Sacks (2000a), we assume a normally distributed family of fibers lying in the $\boldsymbol{e}_c \otimes \boldsymbol{e}_r$ plane. The structure tensor for each fiber is fully defined by the direction

$$\boldsymbol{m}_i := \cos(\theta_i)\boldsymbol{e}_c + \sin(\theta_i)\boldsymbol{e}_r, \tag{6}$$

where $\theta_i \in \mathcal{N}(\mu_f, \sigma_f)$, a normal distribution with mean μ_f and standard deviation σ_f. Herein, we take $\mu_f = 0$ (i.e., mean alignment in the circumferential direction) and let σ_f be a free parameter.

Little information is available regarding the mechanical properties of the Spongiosa, and thus, we assume it behaves like a Neo-hookean material (i.e., $C_{1m} = C_{2m} = C_{1f} = C_{2f} = 0$).

Remark on the fiber model: We follow the discrete Holzapfel fiber model (Holzapfel et al., 2000) as opposed to the continuous one (Holzapfel and Ogden, 2010) because it allows us to explicitly model the individual fiber directions. The latter gives the asymptotic response of the former (i.e., $\lim_{n_f \to \infty}$) in a computationally

[1] These directions orient the tissue sample with respect to the valve organ; c.f. Stella and Sacks (2007) or Sacks et al. (1998).

[2] See Section 4.3 for a discussion.

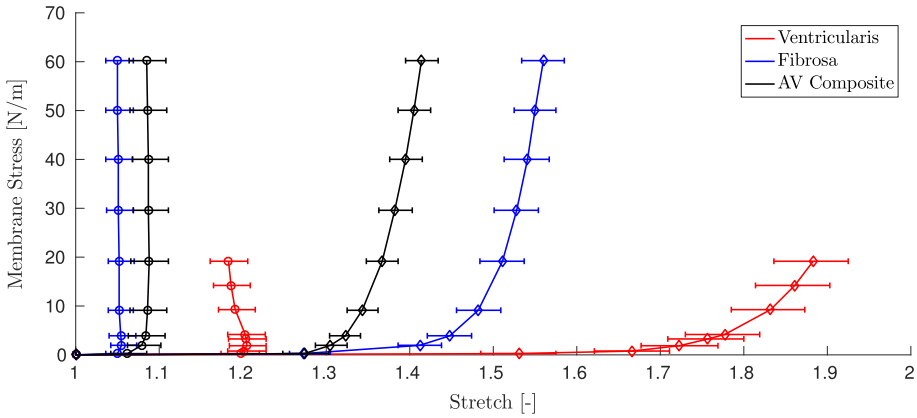

Fig. 1. Aortic valve layer equibiaxial stretch response via (Stella and Sacks, 2007). Circles indicate circumferential response and diamonds indicate radial response.

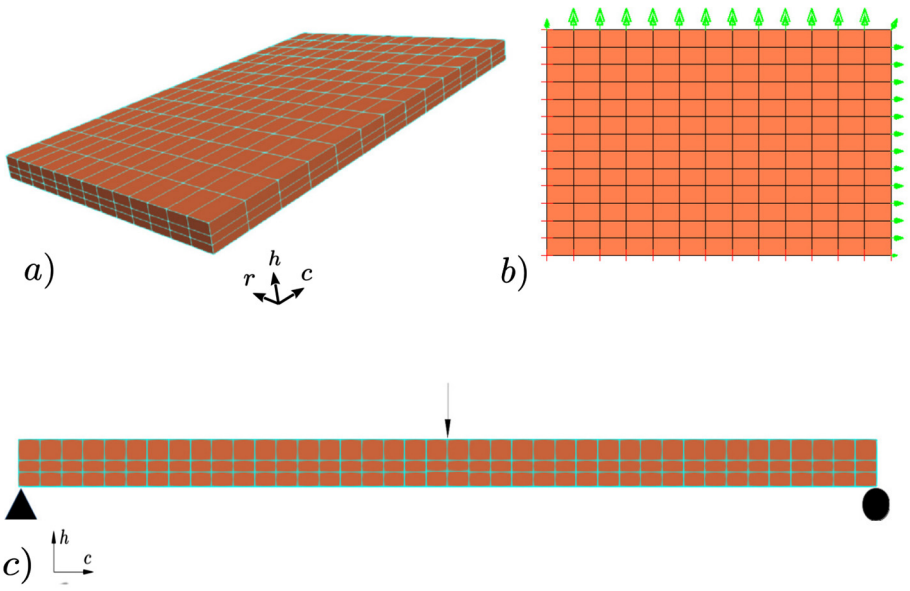

Fig. 2. (a) FEM trilayer tissue model generated with Paraview (Ahrens et al., 2005). (b) 1/4 symmetry FEAP model with boundary displacement and traction boundary conditions. (c) FE bending simulation *a la* Sacks (2001).

efficient manner. We recommend the continuous models (see also Gasser et al., 2006; Freed, 2008) for larger problem sizes (e.g., full aortic valve geometry), but the discrete model provides a more accurate and insightful representation of the fiber micromechanics. Note that unlike the Holzapfel model, we have $(J_4-1)^3$, rather than $(J_4-1)^2$ so that ψ is smooth and twice differentiable (see Appendix C) in the presence of the hinge $(x)_+$.

Remark on viscoelasticity: AV tissue demonstrates viscoelastic behavior when subject to relaxation experiments (Lee et al., 1984). Due to the slow nature of the loading in the referenced experiments, one can safely neglect viscoelasticity.

2.3. Parameter fitting

We consider calibrating the parameters in (3) to experimental data. We first begin by drawing and fixing a set of $n_f = 30$ fibers[3] from $\mathcal{N}(0,1)$, then scale appropriately by $\sigma_f : \mathcal{N}(0,\sigma_f) = \sigma_f \mathcal{N}(0,1)$. The finite-strain parameters $(C_{1m}, C_{2m}, C_{1f}, C_{2f}, \sigma_f)$ are, by construction, negligible for infinitesimal deformation. However, the prestressing engages these parameters and leads to a co-dependence between the finite-strain and infinitesimal-strain (μ and K) parameters. In light of this, we fit the full parameter set in an iterative manner between the small deformation bending and large deformation equibiaxial stretch experiments as follows:

1. Choose an initial value of μ (K is fixed) from Euler-Bernoulli beam bending theory.
2. Fit the finite-strain parameters for each layer with the procedure described in 2.3.1.
3. Determine the necessary prestress for the composite tissue with the procedure described in 2.4.4.
4. Determine μ with the procedure described in 2.3.2.
5. Repeat 2–4 until convergence.

We present a metric in (7) to assess the goodness of fit for the layers and the composite with respect to the equibiaxial stretch experiments.

2.3.1. Equibiaxial stretch

We define a residual sum of squares loss

$$\ell(C) := \sum_{i=1}^{n} (\lambda_c^e - \lambda_c^m(C))_i^2 + (\lambda_r^e - \lambda_r^m(C))_i^2, \tag{7}$$

[3] Our choice of $n_f = 30$ is a balance between accuracy and computational efficiency.

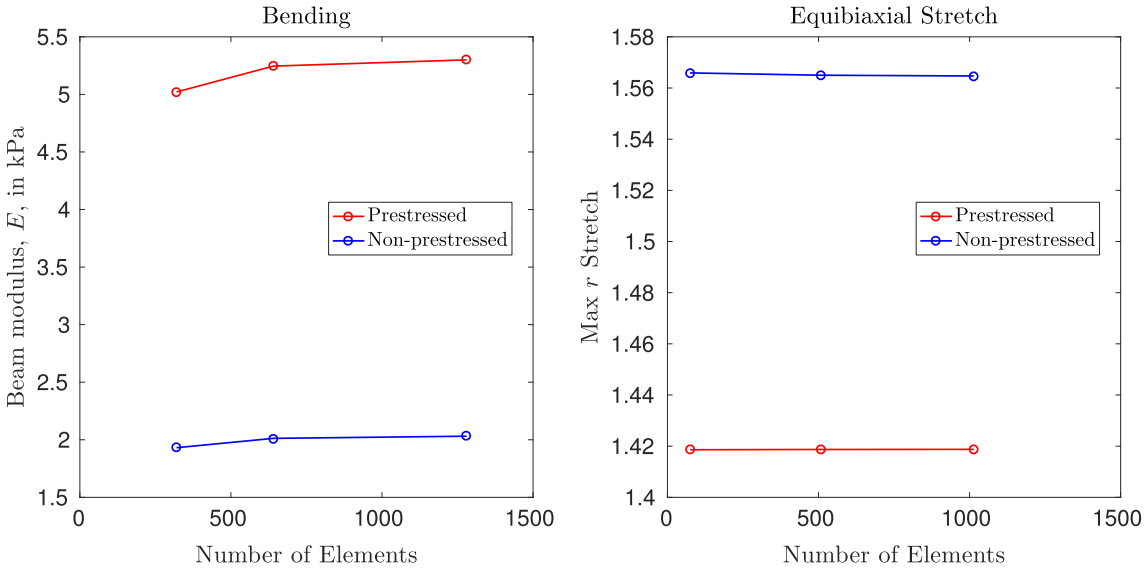

Fig. 3. Convergence studies for AV trilayer FE meshes.

where $C := (C_{1m}, C_{2m}, C_{1f}, C_{2f}, \sigma_f)$, λ is the stretch for a given membrane stress, obtained from the 1st Piola-Kirchhoff stress tensor, and n is the total number of data points; the subscript indicates the direction, and the superscripts e, m denote experimental and model, respectively. We seek the parameters that minimize the nonconvex loss:

$$C^* = \arg\min \ell(C) \text{ subject to } C > 0. \tag{8}$$

Despite the nonconvexity, we can converge to a sufficiently good local minimum using warm-start projected gradient descent with backtracking line-search (Nocedal and Wright, 2006, Chap. 3) implemented in the MATLAB (Mathworks, 2017) package *minConf* (Schmidt, 2008). Because $\ell(C)$ is not an analytical function ($\lambda^m(C)$ is computed from an FE model, detailed in Section 2.4), we estimate the gradients ($\nabla\ell$) with finite differences by probing the FE model with perturbed parameters:

$$\frac{\partial \lambda^m}{\partial C_j} \approx \frac{\lambda^m(C + \delta e_j) - \lambda^m(C)}{\delta}, \tag{9}$$

where $e_j \in \mathbb{R}^5$ is the standard Cartesian basis vector and δ is a suitable differential.

2.3.2. Bending

We fit the infinitesimal-strain parameters to the bending experiment of Sacks (2001), where the AV tissue exhibits linear response over the range of applied deformation. Since we fix the "bulk modulus" $K = 2.2 \times 10^3$ kPa (see Section 2.4.5), all that remains is to fit the "shear modulus" μ such that the bending stiffness is consistent with the values measured by Sacks. We assume all three layers have the same K and μ.

Sacks' bending experiment consisted of $\sim 14 \times 3 \times 0.4$ mm strips of AV tissue that are subject to 3-point bending. Positive and negative midspan deflections were applied with a rigid rod attached to a load cell and the beam deformation field was measured with markers along the edge. The moment-curvature (M versus κ) response was observed to be linear over the range of applied midspan deflections ($\sim \pm 1$ mm), with an effective Young's modulus $E = M/(I\kappa) \approx 5.3$ kPa. Our bending model is described in 2.4.2 where we choose μ such that $M/(I\kappa) \approx 5.3$ kPa. Note that due to the linearity of the response, only a single simulation is needed to determine μ once K has been fixed.

2.4. Finite element modeling

2.4.1. Formulation

We use a finite element (FE) approach to solve (1). Let $\partial\mathcal{B}_u$ and $\partial\mathcal{B}_t$ denote the partitions of the boundary ($\partial\mathcal{B}_0$) of the body, $\mathcal{B}_0$, where deformation and tractions are imposed, respectively, with $\partial\mathcal{B}_u \cap \partial\mathcal{B}_t = \varnothing, \overline{\partial\mathcal{B}_u \cup \partial\mathcal{B}_t} = \partial\mathcal{B}_0$. Eq. (1) is solved by satisfying the weak form statement:

$$\begin{aligned} &\text{Find} && \varphi \in \mathcal{S} := \{\varphi \mid \varphi = \bar{\varphi} \text{ on } \partial\mathcal{B}_u\}, \\ &\text{such that} && \int_{\mathcal{B}_0} \boldsymbol{P} \cdot \nabla(\delta\varphi)\, dV = \cancel{\int_{\mathcal{B}_0} \boldsymbol{B} \cdot \delta\varphi\, dV} + \int_{\partial\mathcal{B}_t} \bar{\boldsymbol{t}} \cdot \delta\varphi\, dA, \\ & && \forall \delta\varphi \in \mathcal{V} := \{\delta\varphi \mid \delta\varphi = \boldsymbol{0} \text{ on } \partial\mathcal{B}_u\}, \end{aligned} \tag{10}$$

where ρ_0 is the material density in $\mathcal{B}_0$ and we assume there is no body force $\boldsymbol{B}$.

2.4.2. Models and boundary conditions

We consider four models: (1) equibiaxial stretch of the fibrosa, (2) equibiaxial stretch of the ventricularis, (3) equibiaxial stretch of the trilayer AV composite, and (4) beam bending of the trilayer AV composite. For all models, we tessellate the domain into 8-node linear brick elements (Fig. 2a) to obtain an approximate numerical solution to (10) using the FE software package FEAP (Taylor and Govindjee, 2017).

The fibrosa and ventricularis equibiaxial stretch model dimensions ($c \times r \times h$) are $11.5 \times 6.3 \times 0.20$ mm and $8.0 \times 5.5 \times 0.15$ mm, respectively, with a mesh size of $13 \times 13 \times 1$. The AV composite equibiaxial stretch model dimensions are $\sim 9.0 \times 6.0 \times 0.46$ mm with a mesh size of $13 \times 13 \times 3$. The AV composite beam dimensions are $14.0 \times 3.0 \times 0.46$ mm with a mesh size of $80 \times 4 \times 12$. A mesh convergence study is given in Fig. 3.

2.4.2.1. Equibiaxial stretch. Stella and Sacks (2007) applied equibiaxial membrane stresses[4] via four discrete points per side and measured the approximately homogeneous strain in the center of the tissue on the surfaces of the fibrosa and the ventricularis. We

[4] Membrane stress here is the force divided by the *initial* length of the edge the force is applied to, i.e., the 1st Piola-Kirchhoff membrane stress.

demonstrate in Appendix D that the overall mechanical behavior of the tissue is not affected by the technical details of these boundary conditions. In fact, we can simply apply uniform normal tractions along the circumferential and radial edges with (1/4) symmetry boundary conditions on the respective opposite edges (Fig. 2b). The nature of the biaxial testing rig forces the three layers to deform together, so we apply stiff spring constraints along the thickness on the boundaries where the traction is applied to ensure that the three layers deform homogeneously in the plane (but heterogeneously out of plane). Motion in the h direction is restrained at the bottom (ventricularis) corners.[5] Note that the boundary conditions apply to the layer models as well as the composite model.

2.4.2.2. Bending. The simply supported bending model is depicted in Fig. 2c. We apply symmetry boundary conditions in the r direction. A midspan deflection is incrementally imposed on the beam and the resulting curvature is computed from a fourth order polynomial fit to the nodal displacements at mid-depth. The prestressing (see Section 3.4) results in an initial curvature κ_0, and thus the moment-curvature response is measured relative to the initial curvature (i.e., M versus $\Delta\kappa$, where $\Delta\kappa = \kappa - \kappa_0$).

2.4.3. Interconnecting fibers

The AV composite tissue is known to act as a single bonded unit (Buchanan and Sacks, 2014). Dissection of the layers reveals interconnecting fibers that span from the fibrosa to the ventricularis (Stella and Sacks, 2007). We model the effect of the interconnecting fibers with perfectly bonded interfaces (i.e., no slip) between adjacent layers.

2.4.4. Prestress

The average AV specimen dimensions from the experiments of Stella and Sacks (2007) are $\approx 9 \times 6 \times 0.5$ mm, $c \times r \times h$ respectively. When separated, the fibrosa (on average) expands to $11.5 \times 7 \times 0.4$ mm and the ventricularis (on average) contracts to $8 \times 5.5 \times 0.2$ mm. We perform the experiment in reverse: we prestress the native stress-free configurations of the layers and attach them (with rigid links) to form the AV composite. The prestressing procedure is summarized as follows:

1. The ventricularis and fibrosa are stretched from their "stress-free" configurations to (approximately) the AV dimensions (as reported by Stella and Sacks (2007)).
2. The layers are then attached and allowed to equilibrate. The AV composite analysis (biaxial stretch and bending) is performed with reference to the attached and equilibrated state.

Remark on prestressing

The fibrosa exhibits a corrugated structure when part of the unloaded AV composite. This geometry is a consequence of a buckling phenomenon in the fibrosa which makes it difficult to determine its true stress-free configuration with the material model we consider here. Thus, we leave the stress-free configuration of the fibrosa as a free parameter in item 1 above. We return to this point in Section 4.

2.4.5. Quasi-incompressibility

AV tissue exhibits quasi-incompressibility (Sacks and Yoganathan, 2007). To obtain a numerically stable, quasi-incompressible material response, we choose a "bulk modulus" of $K = 2.2 \times 10^3$ kPa. Note from (4), K acts as a penalty-like enforcement of $J = \det\boldsymbol{F} \approx 1$. We accordingly use $u - p - \vartheta$ mixed-formulation elements (Malkus and Hughes, 1978). We observe a change of volume well below 1% for the biaxial stretch and bending simulations.

2.4.6. Solution of the nonlinear equations

The static equilibrium FE equations to be solved are posed as a nonlinear vector equation:

$$\boldsymbol{R}(\boldsymbol{u}_t) = \boldsymbol{f}_t, \tag{10}$$

where $\boldsymbol{R}$ are the force resultants of a state of displacements $\boldsymbol{u}_t$ at time t, which must be in equilibrium with the applied nodal forces $\boldsymbol{f}_t$ at time t. We take an iterative Newton-Rhapson approach to solve (10). Given an initial state $\boldsymbol{u}_t^0$, the update equations are

$$\boldsymbol{u}_t^{k+1} \leftarrow \boldsymbol{u}_t^k - \boldsymbol{K}_T^{-1}(\boldsymbol{u}_t^k)\boldsymbol{f}_t, \tag{11}$$

where $\boldsymbol{K}_T = \partial\boldsymbol{R}/\partial\boldsymbol{u}$ is the tangent stiffness, and the iterations are carried out until a stopping criterion, such as the satisfaction of (10) with some tolerance. For the Newton-Rhapson strategy to converge, the initial guess must be in the neighborhood of the solution. This requirement poses an issue for the highly nonlinear AV tissue, particularly in the low stiffness regime. To address this problem, we apply the load incrementally and adaptively. We start with a small load factor α_t ($\boldsymbol{f}_t = \alpha_t \boldsymbol{f}_0$) and adjust the factor heuristically based on the number of iterations (n_i) it takes for (11) to converge ($\alpha_t \propto n_i^{-1}$). In this manner, we are able to circumvent the use of unreasonably small load factors (i.e., excessive computational time) during the entire load path. If a load factor is too large and the Newton-Rhapson algorithm diverges, we appropriately scale the load factor down.

Remark on FE modeling

Note that although we can solve the biaxial stretch problem for the individual layers analytically, the prestressed trilayer AV composite requires a numerical approach.

3. Results

3.1. Mesh convergence

Fig. 3 shows mesh convergence studies for our beam and equibiaxial models for the AV composite system, in both prestressed and non-prestressed states. The mesh densities we use in our study are consistent with converged mesh densities from these plots. The quantities we monitor for convergence are those relevant to the data analysis we are interested in. Note that for brevity we do not show the convergence study for the single layer equibiaxial cases, and simply note they are similar.

3.2. Parameter fitting

The parameter fitting is performed using the equibiaxial data for the AV composite plus the individual layers, together with the bending data. Table 1 summarizes each layer's calibrated finite-strain parameters. Also shown are 95% confidence intervals computed via bootstrap (Efron, 1979) and the convergence curve for the loss $\ell(C)$ per (7) is shown in Fig. 4 top; the loss curves of both layers have the same characteristic shape. Fig. 4 bottom features a perturbation analysis of the fit parameters and demonstrates convergence to a minimum. Note the relative sensitivity of C_{2m}. The individual layer load-deformation curves are presented in Fig. 5 bottom.

We find the moment-curvature response of the bending simulation to be linear, for a midspan deflection loading of ± 1 mm, despite a prestressed initial state (per Section 3.4). We find $\mu = 478$ Pa results in $M/(I\Delta\kappa) \approx 5.3$ kPa.

[5] The corner boundary conditions translate to only one of the four corners for the 1/4 symmetry model.

Table 1
Summary of calibrated model parameters for a normally distributed fiber model with $n_f = 30$; see (3). Fibrosa loss $\ell = 5.13 \times 10^{-4}$ and ventricularis loss $\ell = 8.01 \times 10^{-3}$. 95% confidence intervals computed via bootstrap are reported below the corresponding value. For all layers, $K = 2.2 \times 10^3$ kPa and $\mu = 478$ Pa.

Model	C_{1m} [Pa]	C_{2m} [–]	C_{1f} [Pa]	C_{2f} [–]	σ_f [°]
Fibrosa	4.38 (1.15, 7.15)	8.82 (8.20, 10.40)	18.0 (5.11, 50.72)	1.53×10^3 $(0.76, 1.98) \times 10^3$	6.28 (5.87, 7.59)
Ventricularis	1.13 (0.45, 2.13)	4.11 (3.76, 4.51)	8.68×10^{-2} $(0.24, 40.1) \times 10^{-1}$	46.10 (25.06, 58.67)	8.19 (7.21, 10.53)

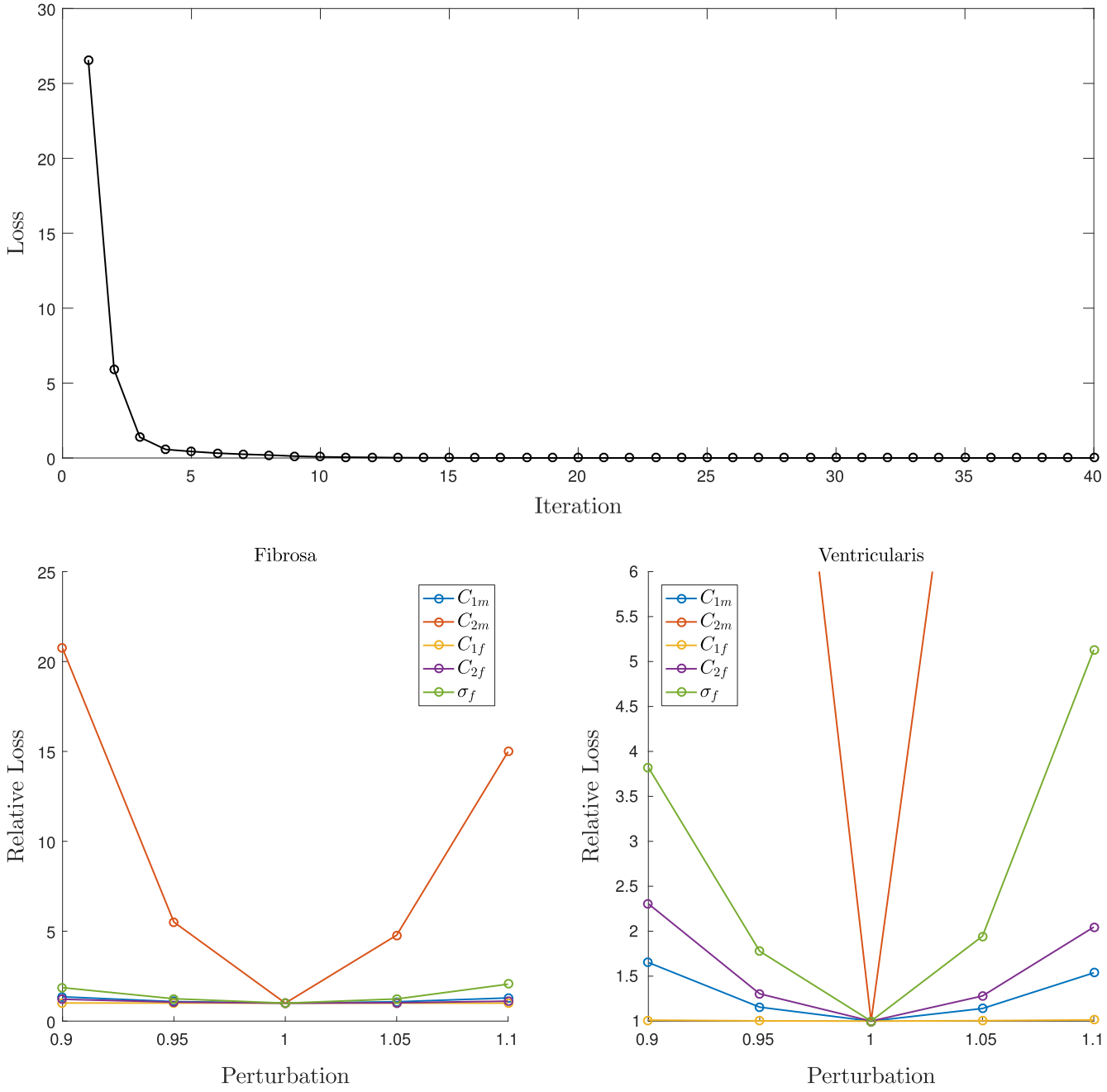

Fig. 4. Top: Convergence of loss (7) using warm-start projected gradient descent with backtracking line-search. **Bottom** Perturbation analysis of parameters for fibrosa (left) and ventricularis (right). For clarity of exposition, the abscissa on the ventricularis plot is truncated.

3.3. Fiber distribution

To illustrate the significance of the fiber distribution model, we present two equibiaxial stretch results for the individual layers: (1) a single family of circumferentially oriented fibers ($n_f = 1, \sigma_f = 0°$ (3)) in Fig. 5 top and (2) a normally distributed family of fibers with $n_f = 30$ in Fig. 5 bottom. Unique parameters are fit for each model. Fig. 6 is a close-up look at the response for low membrane stresses.

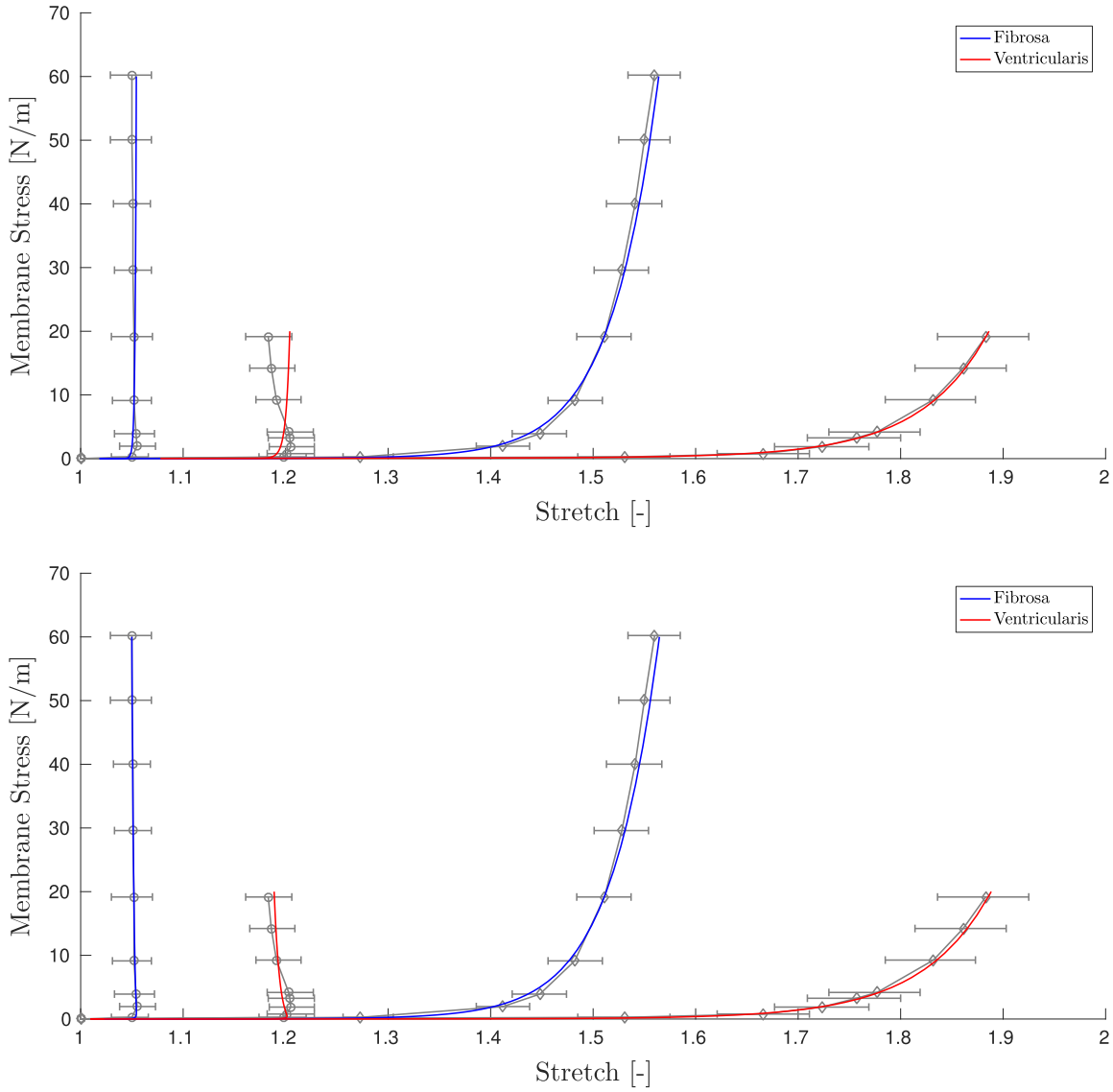

Fig. 5. Equibiaxial stretch response of individual layers plotted against experimental data. The two leftmost curves are the responses in the circumferential direction and the two rightmost curves are the responses in the radial direction. **Top**: Single family of fibers: $n_f = 1, \sigma_f = 0^\circ$. **Bottom**: Distributed family of fibers: $n_f = 30, \sim \mathcal{N}(0, \sigma_f)$, see Table 1 for σ_f values.

We notice $\ell(C)$ goes from 1.01×10^{-3} to 5.13×10^{-4} for the fibrosa and from 2.50×10^{-2} to 8.01×10^{-3} for the ventricularis as we include dispersion in the fiber distribution.

We observe that the single fiber family model fails to capture the "kickback" response, despite being highly anisotropic. The distributed fiber model captures the "kickback" response and boasts a lower loss.

3.4. Trilayer composite biaxial stretch

Next, we look at the equibiaxial stretch response of the trilayer composite, with material parameters per Table 1 and no prestressing, presented in Fig. 7 top. Note the poor fit despite each layer being consistent with its corresponding experiment.

We can reconcile this inconsistency by applying the prestressing procedure outlined in Section 2.4.4. We take the initial configuration of the fibrosa (i.e., the dimensions along the c and r directions) as free parameters, which we tune to obtain the response in the bottom of Fig. 7.

We find that an initial size of $9.05 \times 4.85 \times 0.145$ mm of the fibrosa results in the best response, with a loss $\ell = 1.71 \times 10^{-2}$ (as opposed to $\ell = 1.55 \times 10^{-1}$ for the non-prestressed case). It is worth remarking that due to the nature of our prestressing protocol, the "initial" (i.e., after prestressing but prior to loading) size of the AV specimen is $8.7 \times 5.3 \times 0.46$ mm.

4. Discussion

4.1. Fiber micromechanics

In Fig. 5, we see that AV tissue exhibits a peculiar layer-scale "kickback" behavior in the circumferential direction, wherein increasing load initially results in increasing stretch, followed by a sustained decrease in stretch. We do not observe this behavior when the fibers are oriented in just the circumferential direction (top plot in Fig. 5), despite an anisotropic material specification. We observe the "kickback" behavior in the bottom plot of Fig. 5 when the distribution of fibers is explicitly included.

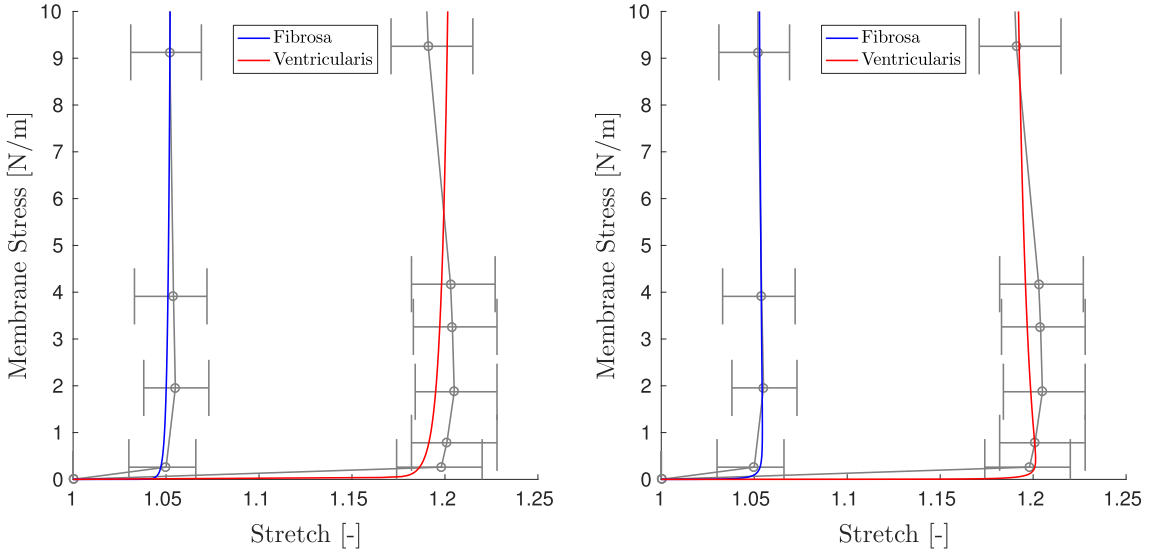

Fig. 6. Close-up of circumferential response in Fig. 5. **Left**: Single family of fibers: $n_f = 1, \sigma_f = 0^\circ$. **Right**: Distributed family of fibers: $n_f = 30, \sim \mathcal{N}(0, \sigma_f)$.

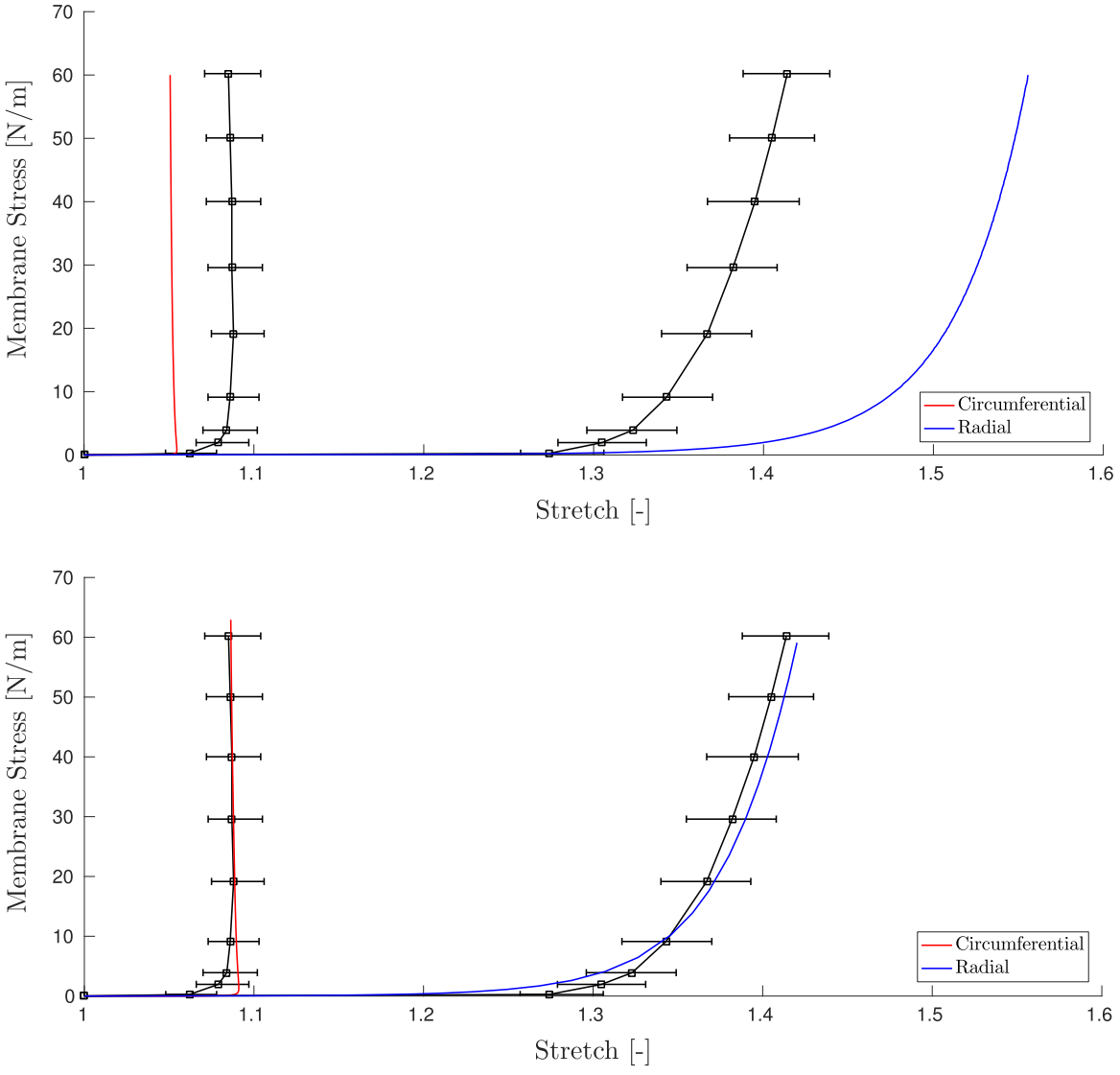

Fig. 7. Equibiaxial stretch response of AV composite tissue with and without prestress, bottom and top respectively.

The "kickback" behavior is a result of the fibers, predominantly aligned in the circumferential direction, rotating into the radial direction, and "transfering" stiffness over. To see this more clearly, consider the deformation gradient at the maximum biaxial loading shown in Fig. 1, $\boldsymbol{F} = \lambda_c \boldsymbol{e}_c \otimes \boldsymbol{e}_c + \lambda_r \boldsymbol{e}_r \otimes \boldsymbol{e}_r + \lambda_h \boldsymbol{e}_h \otimes \boldsymbol{e}_h$, where $\lambda_c < \lambda_r$ are the circumferential and radial stretches, respectively. Take an arbitrary unit vector along a particular fiber, $\boldsymbol{m} = \cos(\theta)\boldsymbol{e}_c + \sin(\theta)\boldsymbol{e}_r$. The orientation of this fiber with respect to $\boldsymbol{e}_c$ is given by θ. The fiber transforms as $\boldsymbol{m}_t := \boldsymbol{F}\boldsymbol{m} = \lambda_c \cos(\theta)\boldsymbol{e}_c + \lambda_r \sin(\theta)\boldsymbol{e}_r$ with the deformation. We can compute the deformed fiber's angle as:

$$|\theta_t| = \left|\operatorname{atan}\left(\frac{\boldsymbol{e}_r \cdot \boldsymbol{m}_t}{\boldsymbol{e}_c \cdot \boldsymbol{m}_t}\right)\right| = \left|\operatorname{atan}\left(\frac{\lambda_r}{\lambda_c}\tan(\theta)\right)\right| > |\theta|, \tag{12}$$

since $\lambda_r/\lambda_c > 1$ and arctangent is a monotonically increasing odd function. Thus, we see a geometric softening in the circumferential direction and a corresponding stiffening in the radial directions, as the fibers rotate under the influence of the applied biaxial loading.

It is possible to capture this behavior with other models. For instance, the general Fung model (Fung, 1990) with appropriate choice of parameters can result in the same behavior for equibiaxial stretch. Our model, however, serves as an intuitive (and heuristic) understanding of the micromechanics by explicitly modeling the discrete fiber directions and tracking their respective rotations. Furthermore, this model allows us to model planar (span$\{\boldsymbol{e}_c, \boldsymbol{e}_r\}$) heterogeneity of the fibers.

4.2. Prestressing

Stella and Sacks (2007) remark on a native prestress in AV tissue, as evidenced by the deformation of the fibrosa and ventricularis post-dissection. We observe that a model that lacks prestressing (Fig. 7 top) fails to capture the AV composite behavior, despite consistent layer-scale behavior. When we apply a prestress (Fig. 7 bottom), we observe a more consistent material response. We conclude that to properly model AV tissue response with layer-scale consistency, prestressing *must* be included.

4.3. Limitations

4.3.1. Prestressing

The main limitation of our model comes from the rather artificial prestressing, in the sense that we do not have the *exact* same before-and-after dimensions as in the experiments of Stella and Sacks (2007). The fibrosa exhibits a corrugated structure when part of the AV composite, but becomes flat when removed, indicating a buckling phenomenon. We contend that to have a fully consistent model, the buckling micromechanics of the collagen fibers in the fibrosa would need to be considered.

4.3.2. Affine fiber transport

We have assumed that the fibers deform affinely, but it is known that this is not always true (Hepworth et al., 2001; Chandran and Barocas, 2006). Further study is required to properly account for non-affine fiber transport.

4.3.3. Equibiaxial stretch

By restricting our attention to equibiaxial stretch experiments, we risk overfitting the model. Indeed, biaxial stretch experiments alone may be insufficient for fully characterizing material response (Holzapfel and Ogden, 2009). However, the lack of consistent layer-specific data for AV tissue leaves few options, though we have incorporated the bending experiments to better capture the true material response. Note that our general modeling framework makes it relatively straightforward to efficiently fit to larger datasets, should they become available.

5. Conclusion

Herein, we presented a method to consistently model AV tissue. We demonstrated the significance of modeling the normal distribution of fibers in the microstructure (in corroboration of the findings of Billiar and Sacks (2000a)). We further demonstrated the need for appropriate prestressing of the AV composite to achieve consistent trilayer mechanical behavior. Our demonstration, however, did not investigate the complex stress state associated with the buckling of the fibrosa in the AV composite, a point that warrants further study.

Conflict of interest

All authors declare that they have no conflicts of interest.

Acknowledgments

We thank the American Heart Association's support via an Innovative Research Grant (MRKM). We also thank Dr. Michael Sacks for the valuable insight he provided us.

Appendix A. Supplementary material

Supplementary data associated with this article can be found, in the online version, at http://dx.doi.org/10.1016/j.jbiomech.2017.06.014.

References

Ahrens, J., Geveci, B., Law, C., Hansen, C., Johnson, C., 2005. Paraview: an end-user tool for large-data visualization. Visual. Handb., 717
Bakhaty, A.A., Mofrad, M.R., 2015. Coupled simulation of heart valves: applications to clinical practice. Ann. Biomed. Eng. 43 (7), 1626–1639.
Balguid, A., Driessen, N.J., Mol, A., Schmitz, J.P., Verheyen, F., Bouten, C.V., Baaijens, F. P., 2008. Stress related collagen ultrastructure in human aortic valves – implications for tissue engineering. J. Biomech. 41 (12), 2612–2617.
Ball, J.M., 1976. Convexity conditions and existence theorems in nonlinear elasticity. Arch. Ration. Mech. Anal. 63 (4), 337–403.
Billiar, K.L., Sacks, M.S., 2000a. Biaxial mechanical properties of the native and glutaraldehyde-treated aortic valve cusp. Part I: A structural constitutive model. J. Biomech. Eng. 122 (4), 327–335.
Billiar, K.L., Sacks, M.S., 2000b. Biaxial mechanical properties of the natural and glutaraldehyde treated aortic valve cusp – Part I: Experimental results. J. Biomech. Eng. 122 (1), 23–30.
Buchanan, R.M., Sacks, M.S., 2014. Interlayer micromechanics of the aortic heart valve leaflet. Biomech. Model. Mechanobiol. 13 (4), 813–826.
Chandran, P.L., Barocas, V.H., 2006. Affine versus non-affine fibril kinematics in collagen networks: theoretical studies of network behavior. J. Biomech. Eng. 128 (2), 259–270.
Dacorogna, B., 2007. Direct Methods in the Calculus of Variations. Springer Science & Business Media, New York, NY.
Efron, B., 1979. Computers and the theory of statistics: thinking the unthinkable. SIAM Rev. 21 (4), 460–480.
Freed, A., 2008. Anisotropy in hypoelastic soft-tissue mechanics, I: Theory. J. Mech. Mater. Struct. 3 (5), 911–928.
Fung, Y., 1990. Biomechanical Aspects of Growth and Tissue Engineering. Springer, New York, NY, pp. 499–546.
Gasser, T.C., Ogden, R.W., Holzapfel, G.A., 2006. Hyperelastic modelling of arterial layers with distributed collagen fibre orientations. J. Roy. Soc. Interface 3 (6), 15–35.
Gundiah, N., Ratcliffe, M.B., Pruitt, L.A., 2007. Determination of strain energy function for arterial elastin: experiments using histology and mechanical tests. J. Biomech. 40 (3), 586–594.
Hepworth, D., Steven-Fountain, A., Bruce, D., Vincent, J., 2001. Affine versus non-affine deformation in soft biological tissues, measured by the reorientation and stretching of collagen fibres through the thickness of compressed porcine skin. J. Biomech. 34 (3), 341–346.
Holzapfel, G.A., 2000. Nonlinear Solid Mechanics. Wiley, Chichester, UK.
Holzapfel, G.A., Gasser, T.C., Ogden, R.W., 2000. A new constitutive framework for arterial wall mechanics and a comparative study of material models. J. Elast. Phys. Sci. Solids 61 (1–3).

Holzapfel, G.A., Ogden, R.W., 2009. Constitutive modelling of passive myocardium: a structurally based framework for material characterization. Philosoph. Trans. Roy. Soc. London A: Math., Phys. Eng. Sci. 367 (1902), 3445–3475.
Holzapfel, G.A., Ogden, R.W., 2010. Constitutive modelling of arteries. Proc. Roy. Soc. London A: Math., Phys. Eng. Sci. 466 (2118), 1551–1597.
Huang, H.-Y.S., Liao, J., Sacks, M.S., 2007. In-situ deformation of the aortic valve interstitial cell nucleus under diastolic loading. J. Biomech. Eng. 129, 880–889.
Katayama, S., Umetani, N., Hisada, T., Sugiura, S., 2013. Bicuspid aortic valves undergo excessive strain during opening: a simulation study. J. Thorac. Cardiov. Sur. 145 (6), 1570–1576.
Labrosse, M.R., Boodhwani, M., Sohmer, B., Beller, C.J., 2011. Modeling leaflet correction techniques in aortic valve repair: a finite element study. J. Biomech. 44 (12), 2292–2298.
Lee, J.M., Courtman, D.W., Boughner, D.R., 1984. The glutaraldehyde-stabilized porcine aortic valve xenograft. I: Tensile viscoelastic properties of the fresh leaflet material. J. Biomed. Mater. Res. 18 (1), 61–77.
MATLAB, 2017. The MathWorks Inc. Natick, Massachusetts.
Malkus, D.S., Hughes, T.J., 1978. Mixed finite element methods – reduced and selective integration techniques: a unification of concepts. Comput. Methods Appl. Mech. Eng. 15 (1), 63–81.
Morrey, C.B. et al., 1952. Quasi-convexity and the lower semicontinuity of multiple integrals. Pacific J. Math. 2 (1), 25–53.
Nocedal, J., Wright, S., 2006. Numerical Optimization. Springer Science & Business Media, New York, NY.
Sacks, M.S., 2001. The biomechanical effects of fatigue on the porcine bioprosthetic heart valve. J. Long-term Effects Med. Implants 11 (3).
Sacks, M.S., Smith, D.B., Hiester, E.D., 1998. The aortic valve microstructure: effects of transvalvular pressure. J. Biomed. Mater. Res. 41 (1), 131–141.
Sacks, M.S., Yoganathan, A.P., 2007. Heart valve function: a biomechanical perspective. Philosoph. Trans. Roy. Soc. B: Biol. Sci. 362 (1484), 1369–1391.
Schmidt, M., 2008. minconf. <http://www.cs.ubc.ca/schmidtm/Software/minConf.html>.
Schröder, J., Neff, P., 2003. Invariant formulation of hyperelastic transverse isotropy based on polyconvex free energy functions. Int. J. Solids Struct. 40 (2), 401–445.
Stella, J.A., Sacks, M.S., 2007. On the biaxial mechanical properties of the layers of the aortic valve leaflet. J. Biomech. Eng. 129 (5), 757–766.
Taylor, R.L., Govindjee, S., 2017. FEAP – Finite Element Analysis Program. <http://projects.ce.berkeley.edu/feap/manual85.pdf>.
Vesely, I., 1997. The role of elastin in aortic valve mechanics. J. Biomech. 31 (2), 115–123.
Weinberg, E.J., Kaazempur Mofrad, M.R., 2008. A multiscale computational comparison of the bicuspid and tricuspid aortic valves in relation to calcific aortic stenosis. J. Biomech. 41 (16), 3482–3487.
Weinberg, E.J., Mofrad, M.R.K., 2007. Transient, three-dimensional, multiscale simulations of the human aortic valve. Cardiovascul. Eng. 7 (4), 140–155.
Weinberg, E.J., Schoen, F.J., Mofrad, M.R.K., 2009. A computational model of aging and calcification in the aortic heart valve. PLoS One 4 (6), e5960.
Weinberg, E.J., Shahmirzadi, D., Mofrad, M.R.K., 2010. On the multiscale modeling of heart valve biomechanics in health and disease. Biomech. Model. Mechanobiol. 9 (4), 373–387.